Applied Magnetic Resonance (2020) 51:1079–1092
https://doi.org/10.1007/s00723-020-01205-1

**Applied
Magnetic Resonance**

ORIGINAL PAPER

EPR Study on the Intercalation of Azoles into Transition Metal Oxides

E. A. Konstantinova[1,2] · **A. I. Kokorin**[3,4] · **A. S. Logvinovich**[5] · **T. V. Sviridova**[5] · **E. N. Degtyarev**[3] · **D. V. Sviridov**[5]

Received: 2 April 2020 / Revised: 11 May 2020 / Published online: 29 May 2020

Abstract

Four azoles of different chemical structure were intercalated into MoO_3, V_2O_5, and WO_3 oxides synthetized via polycondensation of corresponding oxo-acids under the solvothermal conditions. Structural and morphology peculiarities of these hybrid materials were characterized using X-ray and neutron diffraction, electron microscopy and EPR spectroscopy. The EPR measurements provided the evidence that azole molecules coordinate monomers and oligomers of molybdic, tungstic and vanadic acids during the course of solvothermal synthesis of azole-oxide hybrid structures. This coordination is accompanied with reorganization of growing oxide frame leading to the unprecedently high azole loading. As the result, the azole-intercalated layered oxides with high concentration of ordered paramagnetic centers are formed.

1 Introduction

Non-compact structure inherent in the layered polymorphs of molybdenum, tungsten and vanadium oxides makes them effective hosts for intercalation of small organic molecules [1–4]. Moreover, the possibility of combining the synthesis of these transition-metal oxides via polycondensation of oxo-compounds [5] with intercalation of guest molecules facilitates formation of organic-oxide hybrid materials with high degree of intercalation which show much promise as the depot medias (analogues of

---

✉ E. A. Konstantinova
liza35@mail.ru

[1] Physics Department, M.V. Lomonosov Moscow State University, Moscow, Russian Federation

[2] National Research Center “Kurchatov Institute”, Moscow, Russian Federation

[3] N. N. Semenov Federal Research Center for Chemical Physics, Russian Academy of Sciences, Moscow, Russian Federation

[4] Plekhanov Russian University of Economics, Moscow, Russian Federation

[5] Chemistry Department, Belarusian State University, Minsk, Republic of Belarus

the nanocontainer structures). In the case of transition-metal oxides, chemical intercalation is accompanied with coordination of guest molecules that generally leads to the pseudomorphous structural transformations of the oxide host [6, 7].

Intercalative polymerization of aniline, pyrrole or 2,2′-bithiophene in V_2O_5 xerogels was shown to be useful method of synthesis of layered composites of metal-oxide and conductive polymers as a novel electrically conductive material [8]. Since the driving force for such intercalation materials is redox chemistry, the conductivity type appears to be a function of the polymer/V_2O_5 xerogel ratio [8].

Polyaniline was inserted in $V_2O_5{\cdot}nH_2O$ xerogel by oxidative polymerization/intercalation of aniline or anilinium [9]. The interlayer separation (5.6 Å) was consistent with a monolayer of polyaniline chains in the V_2O_5 framework. It was suggested that anilinium is first intercalated and then is oxidatively polymerized in the xerogel upon exposure in air. Upon standing in air, (a) the partial reoxidation of the reduced V_2O_5 framework and (b) further oxidative coupling of anilinium and aniline oligomers occurs inside the V_2O_5 layers. Variable-temperature ^{2}H-wide-line NMR of polyaniline-intercalated $V_2O_5{\cdot}nH_2O$ showed that the polymer chains are sterically confined with respect to phenyl ring rotation. Room-temperature thermoelectric power was negative and depended on the polymer content and the degree of polymerization [9].

A layered V_2O_5 structured xerogel was synthesized via a hydrothermal method from commercial V_2O_5 powder and graphene: $V_2O_5{\cdot}nH_2O$ xerogel composites were then prepared [10]. Structure and morphology were investigated and heat treatment at different temperatures yielded compounds with different graphene loading. In $V_2O_5{\cdot}nH_2O$, the phase transformation occurs similar to those in the bare V_2O_5. The vanadium oxide xerogel is built of layers *ca.* 100 nm in width. Increase of the graphene content in the composites results in better cycling stability under testing as cathodes in lithium ion batteries. The outstanding electrochemical performance were attributed to the grapheme-induced special structure and morphology [10].

Novel anion exchange hybrid materials were prepared by the intercalating polydiallymethylammonium chloride (P1) or poly-allylamine hydrochloride (P2) polyelectrolytes into V_2O_5 [11]. It was shown that the interlayer space of V_2O_5 expands from 0.44 to 1.40 nm and 1.80 nm upon intercalation of P1 and P2, respectively. X-ray photoelectron spectroscopy revealed that some V^{5+} centers were reduced to the V^{4+} state during the intercalation. The interlayer separation was consistent with the formation of coiled conformation of the polycations. The resultant hybrid materials retain *ca.*45% and 37% of chloride ions still available for anionic exchange, respectively. These materials were used to encapsulate a cyanine anionic dye [11].

Ionic liquid has been used to modify two-dimensional (2D) layered transition-metal dichalcogenide (TMDCs) crystals which revealed properties not seen in the bulk materials [12]. In the case of TMDC-based transistor structures, the ionic liquid led to ion intercalation when the ion size of 'gate' electrolyte was small compared to the interlayer one. The time-dependent source-drain resistances of thin crystals showed the effect of ion intercalation, and the correlation between the ion occupation of allowed interstitial sites and the device characteristics [12].

The structural, physical and chemical properties of layered transition-metal oxides were as two-dimensional (2D) systems were reviewed in detail in [13]. With the use of 2D ultrathin vanadyl phosphate ($VOPO_4$) nanosheets as a model material, an interlayer engineering strategy employing controlled intercalation of organic molecules was proposed. These materials are promising for lithium ion batteries and, seems, have potential for large-scale energy storage systems [14].

Very recently, the MXenes demonstrated outstanding properties due to their highly active hydrophilic surfaces coupled with high metallic conductivity based on the intercalation between $Ti_3C_2T_x$ (T_x describes the surface termination) [15]. Thus, it has been shown that the capacitance and charge carrier kinetics in the case of $Ti_3C_2T_x$ MXene electrodes exhibit drastic enhancement after urea intercalation. Such improvement was attributed to the urea intercalation-induced changes in the $Ti_3C_2T_x$ surface chemistry [15].

The outstanding effectiveness of nanocontainer depot systems based on benzazole-loaded mesoporous oxides as the corrosion protection and metal surface healing systems was demonstrated recently [16–18].

The intercalation of organics into lamellar transition-metal oxides can be thus considered as a powerful tool for design and engineering of hybrid materials. Due to redox activity inherent into transition-metal oxides which is responsible for production of paramagnetic centers (PCs) as the result of coordination in the oxide frame, the electron paramagnetic resonance (EPR) spectroscopy makes it possible a direct investigation of the interaction between intercalated molecules and oxide matrix accompanied with the intercalation-induced phase transitions.

In this work, we have employed EPR spectroscopy to investigate the interactions arising between hexagonal MoO_3 (h-MoO_3), hexagonal WO_3 (h-WO_3) and layered V_2O_5 matrixes, on the one hand, and different azoles, including benzotriazole (BTA), benzoimidazole (BIA), 2-aminotriazole (2ATA), and tetrazole (TA), on the other hand, to elucidate their role as a key factor, governing the intercalation-induced transformations of oxide matrix that facilitates the adaption of the solvothermally derived oxide host to the incorporation of guest molecules.

2 Experimental

2.1 Synthesis of Azole-Intercalated Oxides

For preparation of h-MoO_3, h-WO_3 and layered V_2O_5 as well as azole-intercalated hybrid structures on their basis, the solvothermal synthetic technique [5] was employed. In all cases, as the oxide precursor corresponding oxo-acids obtained by ion-exchange method (i.e., via acidification of sodium molybdate, sodium tungstate or sodium vanadate at the resin) were used. The synthesis of oxide dispersions was carried out through the incubation of aqueous solutions of oxo-acids (starting concentration in all cases was 0.2 mol/L) at 100 °C for 4 h under continuous stirring (the reaction volume was maintained constant throughout the incubation). To obtain azole-oxide hybrids, BTA, BIA, 2ATA, or TA (see the structures given in Fig. 1) were dissolved in the water–ethanol mixture and added to the reactant solution before synthesis. In all cases, the azole concentration was 10 g/L. The resultant

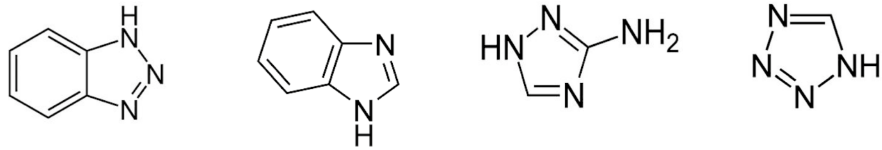

Benzotriazole (BTA) Benzoimidazole (BIA) Aminotriazole (2ATA) Tetrazole (TA)

Fig. 1 Structures of the azoles used for preparation azole-intercalated hybrids

precipitate was collected by centrifugation and thoroughly washed with water–ethanol (1:1) mixture to remove residual azoles.

The azole loading in thus synthesized organic-oxide hybrid materials given in Table 1 was evaluated spectrophotometrically by dissolving oxide matrix in NH_4OH (25% aqueous solution) + ethanol mixture (1:9). It is apparent that the amount of azole substances incorporated into the MoO_3 matrix is governed mainly by the size of the guest molecules and the number of N-atoms capable of coordination in the oxide host. Thus, as evident from Table 1, the most effective intercalation is observed in the case of relatively small molecules of 2ATA (56 mol %) and TA (43 mol%) with large number of N-atoms which can be involved in the formation of non-covalent bonds (including hydrogen ones).

2.2 Structural and Morphological Characterization of Azole-Intercalated Oxides

The crystal structure of azole-intercalated oxides was assigned by X-ray diffraction on a PANalytical Empyrean instrument with Cu K_α radiation ($\lambda = 1.54178$ Å). The XRD analysis evidenced that intercalation accompanying the growing of oxide matrix results in the phase segregation and, as the result, initial hexagonal MoO_3 exhibits partial conversion into anorthic MoO_3, whereas hexagonal WO_3 transforms into the mixture of two orthorhombic polymorphs; similarly, monoclinic V_2O_5 exhibits conversion into orthorhombic V_4O_9 phase with the admixture of monoclinic V_5O_{12} phase. The typical XRD patterns for BTA-intercalated transition-metal oxides are given in Fig. 2.

To ensure the exact identification of the phases arising due to pseudomorphous structural transformations of the oxide host resulted from the azole intercalation, the neutron diffraction measurements were performed using the High-Resolution

Table 1 Concentration of azoles intercalated into metal oxides

Azole-oxide hybrid structure	Azole loading, mol%
MoO_3:BTA	41.0
WO_3:BTA	4.6
V_2O_5:BTA	4.1
MoO_3:2ATA	56.0
MoO_3: BIA	25.0
MoO_3:TA	45.0

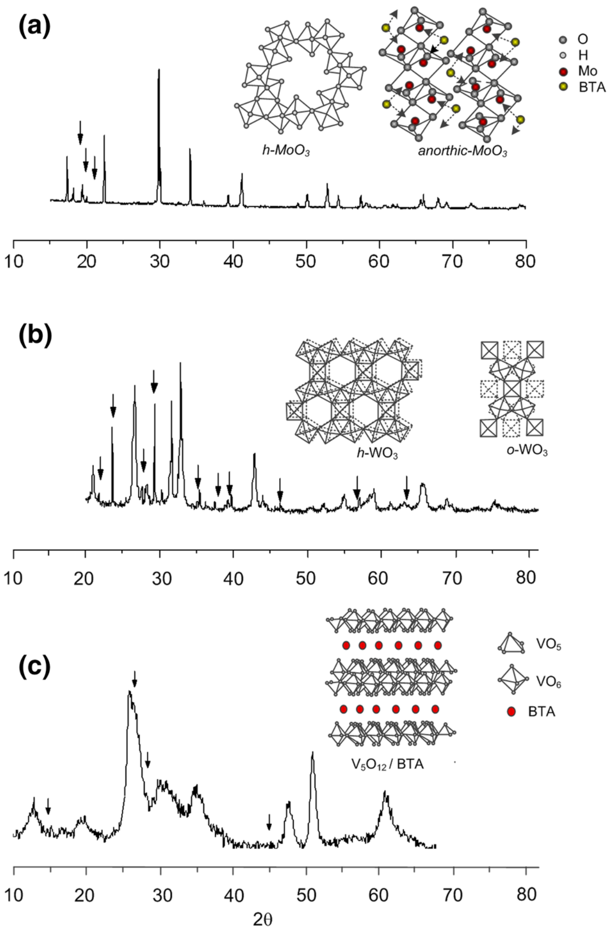

Fig. 2 **a** XRD pattern of BTA-intercalated MoO_3.The reflexes in the pattern are related to hexagonal and anorthic MoO_3 phases (the reflexes corresponding to the anorthic MoO_3 are indicated by arrows). The structure representations of hexagonal and anorthic MoO_3 are given in the insertion. **b** XRD pattern of: BTA-intercalated WO_3. The reflexes in the pattern correspond to the orthorhombic WO_3 (a mixture of two pseudopolymorphs with structures similar to those of hydrated oxide forms *o*-$WO_3{\cdot}H_2O$ (indicated by arrows) and *o*-$WO_3{\cdot}0.33H_2O$).The structure representations of initial hexagonal WO_3 and orthorhombic WO_3 arising as the result of intercalation are given in the insertion. **c** XRD pattern of BTA-intercalated V_2O_5. The reflexes in the pattern correspond to the orthorhombic phase V_4O_9 with the admixture of monoclinic V_5O_{12} (the latter is indicated with arrows). The structure representation of orthorhombic V_4O_9 is given in the insertion

Fourier Diffractometer at IBR-2 pulsed reactor (Joint Institution for Nuclear Research, Dubna, Russia). To minimize the neutron scattering by protons, the samples of azole-intercalated oxides were treated before neutron diffraction experiments at 45 °C for 3 days to ensure their dehydration (the structural water content was evaluated by TG analysis from 25 to 500 °C using a TG-DSC analyzer NETZSCH STA 449 Jupiter); however, high hydration degree inherent in V_2O_5 and hybrid structures on its basis plagues registration of neutron diffraction in their case. The neutron diffraction patterns (Fig. 3) strongly confirm formation of anorthic MoO_3 and orthorhombic WO_3 upon intercalation.

The morphological investigations of bare and azole-intercalated oxides were performed employing LEO 1420 SEM microscope. The SEM images evidenced that solvothermal synthesis yields the micron-sized regular prismatic (in the case of MoO_3) or tablet-like (in the case of WO_3 and V_2O_5) crystallites (Fig. 4).

The polycondensation of oxo-acids in the presence of BTA yields distorted and highly irregular tablet-shaped particles which, however, preserve crystalline structure (Fig. 4). The SEM images given in Fig. 4 also suggest that coordination of 2ATA molecules occurring in the interlamellar space is accompanied with degradation of solvothermally derived oxide crystallites leading to the formation of sheet-like particles. The XRD patterns (not shown) evidence that resultant 2ATA-intercalated oxide host consists of the mixture of hexagonal and anorthic MoO_3 phases. On the other hand, the TA molecules exhibiting the prominent coordination tendency coordination can interact with oxo-oligomers already at the initial stages of the solvothermal synthesis thus hampering the recrystallization of growing oxide into hexagonal polymorph and the whiskers of monoclinic MoO_3 appears to be the main product of synthesis in this case. In contrast, the incorporation of BTA molecules having aromatic ring in their structure occurs less effective (the loading was found to be 41 mol%), whereas the lack of N-centers responsible for coordination in the case of BIA results in further decrease of intercalation efficiency (the loading does not exceed 25 mol%). Note that due to low loading values, the structure of MoO_3 particles exhibits only a mere distortion upon intercalation as evident by XRD analysis.

2.3 EPR Measurements

The EPR spectra were recorded on a Bruker ELEXSYS-E500 spectrometer (*X*-band, the sensitivity up to 10^{10} spin/G) at 77 K. We have used modulation frequency equal to 100 kHz and the microwave power of 0.2 mW. Concentrations of paramagnetic

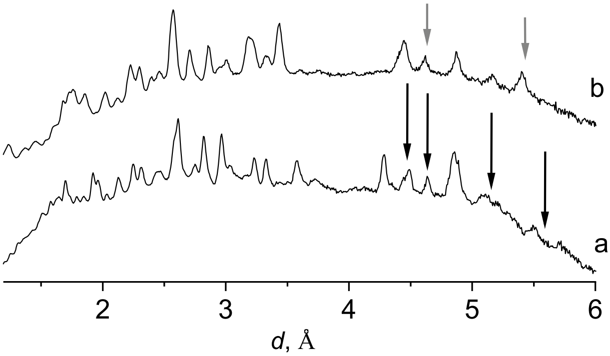

Fig. 3 Neutron diffraction patterns of **a** MoO_3:BTA and **b** WO_3:BTA. Black arrows indicate reflexes corresponding to anorthic MoO_3, gray arrows indicate orthorhombic WO_3; the remaining reflexes are related to the *h*-MoO_3 (curve *a*) and orthorhombic WO_3 (curve *b*)

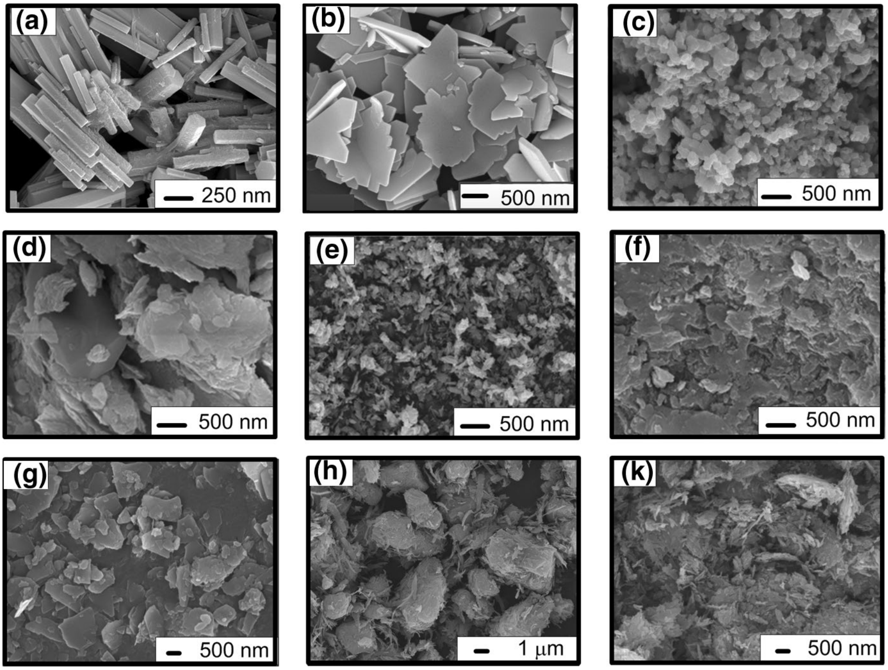

Fig. 4 SEM images of microcrystals of **a** *h*-MoO_3, **b** *h*-WO_3, **c** V_2O_5, **d** MoO_3:BTA, **e** WO_3:BTA, **f** V_2O_5:BTA, **g** MoO_3:2AMT, **h** MoO_3: BIA; **k** MoO_3:TA

centers were evaluated by double integration of the spectrum and it comparison with that one of $CuCl_2{\cdot}2H_2O$ crystal with known number of spins used as the standard. To determine the *g*-factor values of PCs, paramagnetic centers the EPR spectra simulations were carried out with the use of EasySpin MATLAB toolbox [19].

3 Results and Discussion

3.1 Effect of the Nature of Metal Oxides

Both the nature of metal oxide and structure of intercalated azole can be considered as the key factor affecting the EPR behavior of organic-oxide hybrid materials The role of the first factor was investigated using a family of BTA-intercalated transition-metal oxides. Typical EPR spectra of bare *h*-MoO_3 and *h*-WO_3 as well as MoO_3:BTA and WO_3:BTA hybrid structures are given in Fig. 5. The main signal locating between 360 and 380 mT belongs to the Mo^{5+} centers; the determined spin-Hamiltonian parameters of these PCs are presented in Table 2. Comparison of gained parameters with data known from the literature [20–23] confirms that we observe really Mo^{5+} PCs in MoO_3. Figure 5 evidences that the intercalation of BTA results in *ca*. fivefold increase of the signal intensity in parallel with a fact that the

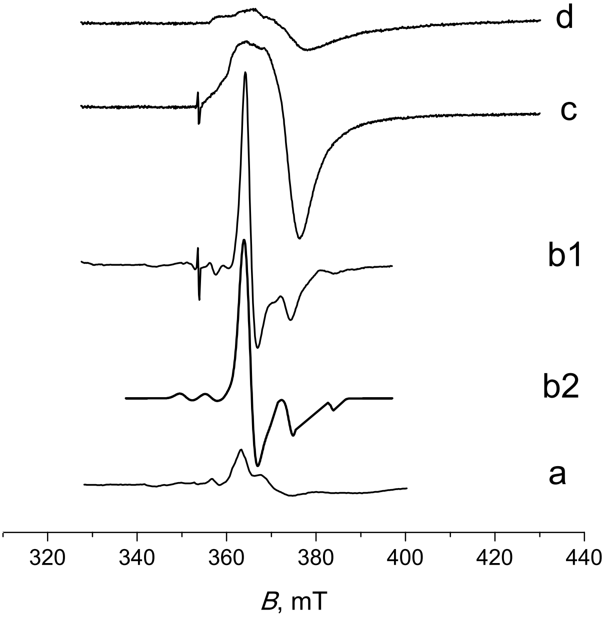

Fig. 5 EPR spectra of **a** bare *h*-MoO_3, **b** MoO_3:BTA hybrid structure, **c** *h*-WO_3, and **d** WO_3:BTA hybrid structure at 77 K. (*b*2) is a simulated spectrum

Table 2 EPR parameters of the samples studied. $S = 1/2$. $I = 5/2$ (Mo^{5+}). $I = 7/2$ (V^{4+})

Sample	Magnetic parameters	PC content, spin/g
MoO_3	$g_1 = 1.948$, $g_2 = 1.913$, $g_{\|} = 1.815$	$6.1 \cdot 10^{17}$
MoO_3:BTA	$g_{\perp} = 1.934$, $g_{\|} = 1.889$, $g_S = 2.000$	$3.1 \cdot 10^{18}$
MoO_3:BIA	$g_{\perp} = 1.952$, $g_{\|} = 1.937$	$2.65 \cdot 10^{19}$
MoO_3:TA	$g_1 = 1.955$, $g_2 = 1.945$, $g_{\|} = 1.921$, $g_S = 1.9997$	$1.45 \cdot 10^{19}$
MoO_3:2ATA	$g_1 = 1.942$, $g_2 = 1.929$, $g_{\|} = 1.917$, $g_0 = 2.251$, $\Delta H_0 = 12.0$ mT	–
WO_3	$g_1 = 1.973$, $g_2 = 1.933$, $g_3 = 1.888$	$5.0 \cdot 10^{17}$
WO_3:BTA	$g_{\perp} = 1.898$, $g_{\|} = 1.943$, $g_S = 2.000$, $\Delta H_S = 0.3$ mT	$4.2 \cdot 10^{18}$
V_2O_5	$g_{\perp} = 1.986$, $g_{\|} = 1.934$, $A_{\perp} = 7.7$ mT, $A_{\|} = 20.3$ mT	$2.2 \cdot 10^{19}$
V_2O_5:BTA	$g_0 = 1.971$, $\Delta H_0 = 12.8$ mT	$6.7 \cdot 10^{19}$

spectrum became much more individual. Double integration of the EPR spectrum gives the total concentration of Mo^{5+} centers which is listed in Table 2.

The *g*-tensor values of MoO_3:BTA sample are shifted from those of Mo^{5+} PCs out of measurement errors what indicates changes of the Mo^{5+} PCs structure and in its local environment. It is also seen from Fig. 5 that a very narrow low-intensity single line with $g_S = 2.000 \pm 0.003$ and a linewidth $\Delta H_S = 0.3 \pm 0.02$ mT arises in the spectrum of MoO_3:BTA hybrid material. Taking into account the parameters of this singlet line, one can attribute it to the organic radical species produced during formation of organic-oxide hybrid structure and stabilized in the oxide matrix.

The signal from W^{5+} PCs in the case of bare *h*-WO_3 and WO_3:BTA are observed in EPR spectra (Fig. 5) at similar magnetic fields, and their parameters are shown in Table 2. A signal corresponding to the organic radical is also detected in case of BTA intercalation into WO_3 matrix but shows lower intensity as compared to MoO_3:BTA (Fig. 5; Table 2).

Typical EPR spectrum of solvothermally derived layered V_2O_5 is shown in Fig. 6. The spin-Hamiltonian parameters of V^{4+} centers, which are the source of EPR signal, are given in Table 2. Comparison of the determined parameters with the data available from the literature allows us to attribute these PCs to paramagnetic $O{=}V^{2+}$ centers with $g_{\|}<g_{\perp}$ which possess the structure of the distorted square bipyramide; these PCs are described in detail by many researches [24–32 and Refs therein].

Intercalation of only 4 mol% of BTA causes drastic changes in EPR spectrum (Fig. 6) which becomes mainly a singlet with very small residual components with positions typical of the isolated PCs (*cf.* with the spectrum from bare V_2O_5 prepared via solvothermal synthesis). This single line has the following parameters: $g_V = 1.971 \pm 0.003$ and $\Delta H_V = 13.2 \pm 0.3$ mT. Such hfs-structure-free spectrum points to the aggregation of V^{4+} centers yielding clusters with a strong electron spin exchange interaction among the PCs [22, 33]. We have compared a value of g_V which is in excellent agreement with an isotropic constant $g_0 = (g_{\|} + 2\ g_{\perp})/3 = 1.969$ calculated from parameters $g_{\|}$ and $g_{\perp}$ given in Table 2. This permits us to conclude that the nature and structure of corresponding PCs, both isolated and aggregated, are identical. A signal from organic radical species is not observed in this case due to its low intensity as compared to the signal produced by V^{4+} centers.

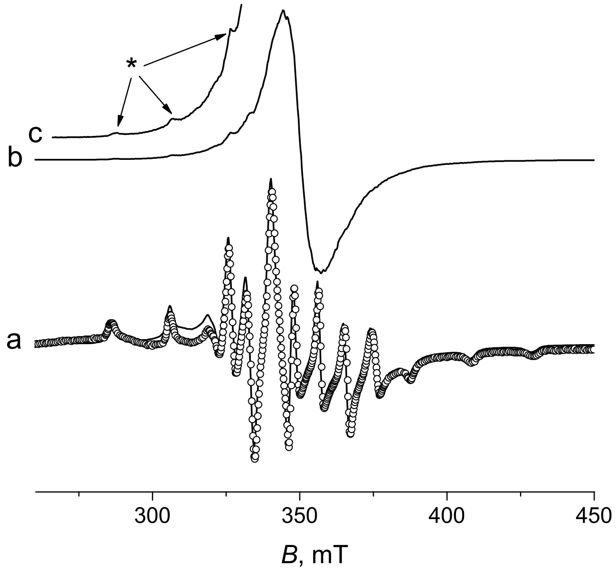

Fig. 6 EPR spectra of **a** bare V_2O_5 (solid line) and **b** V_2O_5:BTA hybrid structure at 77 K. Spectra are normalized by the amplitude. Curve **c** is the fivefold enlarged section of spectrum **b**; asterisk and arrows indicate lines demonstrated by spectrum **a**. Open circles represent a simulated spectrum **a**

Double integration of EPR spectrum for isolated PCs (spectrum *a* in Fig. 6) and aggregated ones (spectrum *b* in Fig. 6) yields the following values for concentration of isolated and aggregated V^{4+} centers: $(2.2 \pm 0.2) \times 10^{19}$ and $(6.7 \pm 0.7) \times 10^{19}$ spin/g, respectively. The insertion of BTA molecules thus results in the *ca*. three-fold increase in V^{4+} concentration that, however, is not enough to ensure the observed singletization of the EPR spectrum. It can be thus assumed that BTA intercalation should led to serious structure reorganization resulting in formation of aggregates with high local concentration of V^{4+} centers which initially were homogeneously distributed in the oxide matrix. We should note that one can easily calculate the total content of vanadium atoms $[V^{n+}]_0$ equal to *ca*. $(6.6 \pm 0.7) \times 10^{21}$ atom/g, i.e., only approximately 1% of vanadium ions in bare V_2O_5 are paramagnetic ones, whereas remaining 99% are diamagnetic and cannot be detected by EPR technique.

The EPR spectra given in Figs. 5, 6 evidence that there exists a strong interaction between intercalated BTA molecules and oxide frame resulting in the formation of the charge-transfer complexes. However, due to the differences in the mechanism of polycondensation of molybdic, tungstic, and vanadic acids, these interactions affect the growing of oxide matrixes in quite different manners. Thus, the prolonged induction period typical for polycondensation of molybdic acid [5] creates favorable conditions for complexation of its monomers and small oligomeric species. According to XRD and neutron diffraction analysis (the diffraction patterns are given in Figs. 2, 3), such complexation of precursors of the oxide matrix with BTA molecules results in the formation, along with the hexagonal phase, also the anorthic (triclinic) one, the concentration of the latter polymorph in the resultant MoO_3:BTA hybrid material being below 15%. Both polymorphs possess a layered structure and are able to incorporate BTA molecules in the interlamellar spacing in the case of anorthic phase and both in the interlamellar domain and within the hexagonal channels in the case of hexagonal phase (the BTA loading amounts 41 mol%—Table 1). In this case, Mo^{5+} centers generated as the result of interaction of BTA molecules with matrix oxide appears to be almost homogeneously distributed in the MoO_3 frame and behave as individual ones as evident by Fig. 5.

In contrast to the solvothermal synthesis of *h*-MoO_3, the growing of layered V_2O_5 via polycondensation occurs through the formation of colloidal hydrated oxide [5, 34]. The binding of V_2O_5 particles with BTA affects their further aggregation and, as evident by XRD analysis (Fig. 2), the mixture of monoclinic V_2O_{15} (~60%) and orthorhombic V_4O_9 (~30%) is formed instead of monoclinic V_2O_5 (so-called lamellar ‘xerogel’ phase [35]) that normally crystallizes from aqueous solution of vanadic acid in the absence of BTA. Trapping of BTA molecules occurs exclusively in the interlamellar volume of monoclinic phase that results in high local concentration of V^{4+} centers which thus exhibit aggregation, the manifestations of which are observed in the EPR spectrum (Fig. 6).

Under solvothermal conditions, tungstic acid exhibits rapid spontaneous polycondensation [5, 36] due to which the growing of the oxide phase occurs through aggregation of large building blocks of hydrated oxide followed by the precipitate recrystallization [5]. The substitution of the coordinated water in the hydrated tungsten oxide forces their crystallization in orthorhombic polymorph as evident by XRD and neutron diffraction patterns given in Figs. 2, 3. The formation of orthorhombic structure resulting from the shift of oxide lamellae relative to each other can be attributed to the bidentate nature of BTA molecules as the complexing agent. However, the orthorhombic WO_3 matrix provides only limited number of positions for intercalation of guest molecules (Table 1 evidences that BTA loading in the case of WO_3:BTA hybrid material of orthorhombic structure is much lower as compared to MoO_3:BTA hybrid material exhibiting the hexagonal/anorthic structure). Coordination of BTA molecules forming bridges between oxide lamellae is accompanied with formation of stabilized organic radical species; however, due to widening of EPR lines as the result of the effective charge delocalization in the oxide blocks, the manifestations of the W^{5+} centers in the EPR spectrum of WO_3:BTA hybrid structure appears to be insignificant.

3.2 Effect of Structure of the Incorporated Azole Molecules

To elucidate the role of the chemical structure of guest molecules in the formation of azole-intercalated metal oxide and their functional behavior, we have studied and compared the effect of four different intercalating agents (Fig. 1). Figure 7 represents EPR spectra recorded at 77 K in a wide range of magnetic field for MoO_3 oxide intercalated with BIA, 2ATA, and TA. One can see from Figs. 5, 7 that obtained EPR spectra differ as to their shape and spin-Hamiltonian parameters (Table 2). This points to the fact that hybrid structures arising as the result of intercalation of these four azoles are not the same as to their micro-environmental and spatial organization. Also, the PCs content in these intercalated systems differs also up to eightfold. In principle, the observed effects could be explained taking into consideration differences in the chemical structure and in the complex-forming behavior of azoles used. Taking into account the spectrum shape and EPR parameters, we can assume that TA molecules form the structures with Mo^{5+} ions rather similar to those observed in the case of BTA, while very intensive line at *ca*. 352.7 mT (x–y orientation in the external magnetic field, Fig. 7) in the case of MoO_3:BIA sample seems to reflect either the existence of several coordination structures or/and domains with very high local concentration of Mo^{5+} PCs. Note that in no one case except BTA, signals from organic radicals were observed.

The most intriguing is the appearance of the broad single line with $g_0=2.251$ and the line width $\Delta H_0=12.0$ mT in the case of MoO_3:2ATA superimposing with a residual spectrum similar to the isolated Mo^{5+} PCs in MoO_3. Such broad single lines are characteristic for metal-oxide systems containing nanoparticles with ferromagnetic interaction between metal ions [37–41]. One can expect that due to lamellar structure of the oxide host and high 2ATA loading (Table 1), a layered ‘metal ion-coordinated azole ligand’ structure with long range ordering providing the parallel orientation of spins is formed which could be similar to Cu(II)-tetrazole complexes demonstrating ferromagnetic coupling at low temperatures [42].

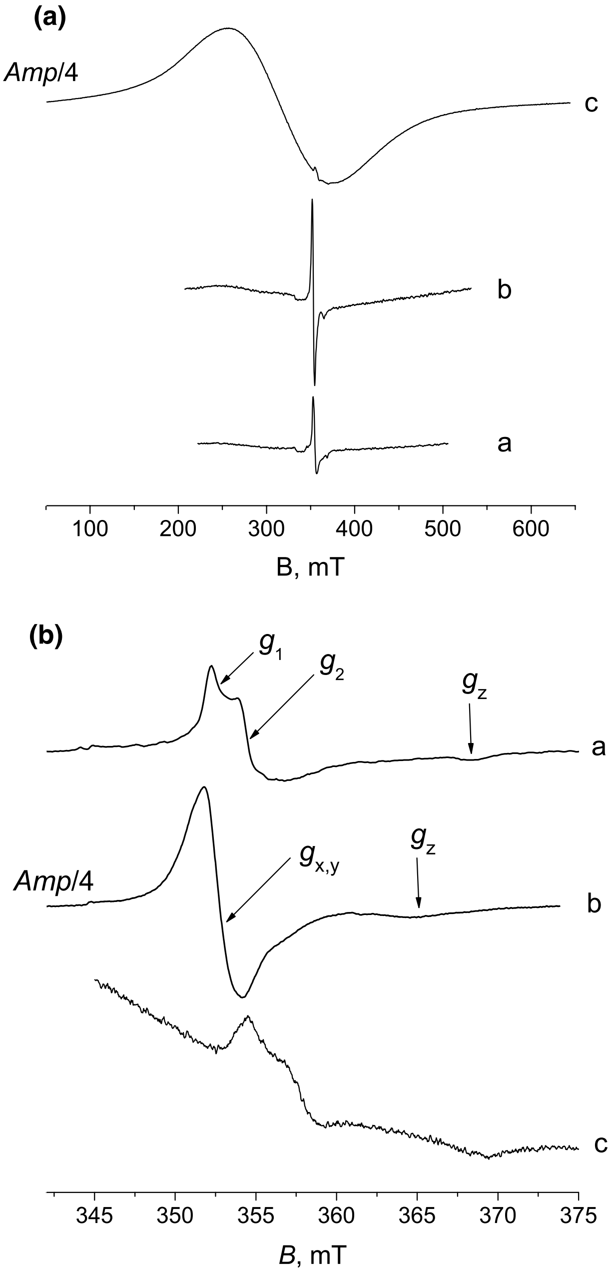

Fig. 7 EPR spectra of **a** MoO_3:TA, **b** MoO_3:BIA, and **c** MoO_3:2AMT at 77 K at two scales of the magnetic field. The amplitude of spectrum **c** is fourfold decreased comparing to other spectra

4 Conclusions

The EPR measurements provide an evidenced that azole molecules coordinate monomers and oligomers of molybdic, tungstic and vanadic acids during the course of solvothermal synthesis of azole-oxide hybrid materials. This coordination is strong enough to be accompanied with charge transfer effects and leads to the reorganization of growing oxide frame which thus appears to be adapted to the incorporation of guest molecules. The unprecedently high azole loading (up to 56 mol%) attained in the case of solvothermally derived azole-intercalated transition-metal oxides yields complex lamellar composites with high concentration of ordered paramagnetic centers.

Author Contributions AIK Supervision, validation, writing–reviewing. ASL visualization, investigation. TVS investigation, data curation. YND investigation, software. EAK investigation, editing. DVS conceptualization, methodology, writing–original draft preparation. All authors approve the final version of the manuscript.

Funding T.V.S, A.S.L. and D.V.S. acknowledge the support from the Belarusian Republican Foundation for Fundamental Research (Grant Kh19MS-017). A.I.K. and E.A.K. are thankful for the financial support to the Russian Foundation for Basic Research (Grant № 18-53-00020-Bel-a).

Data and Materials All data needed to evaluate the conclusions in the paper are present in the paper.

Compliance with Ethical Standards

Conflict of interest The authors declare no competing interests.

References

1. M. Atsharpur, A. Mahjoub, M.M. Amini, J. Inorg. Organomet. Polym. Mater. **19**, 298 (2009)
2. Y. Jing, Q. Pan, Z. Cheng, X. Dong, Y. Xiang, Mater. Sci. Eng. B **138**, 55 (2007)
3. T. Rostamzadeh, K. Riché, S.S. Akbarian-Tefaghi, T.T. Brown, J.B. Wiley, FlatChem **5**, 9 (2017)
4. J.W. Johnson, A.J. Jacobsen, S.M. Rich, J.F. Brody, J. Am. Chem. Soc. **103**, 5246 (1981)
5. T.V. Sviridova, L.I. Stepanova, D.V. Sviridov, in *Molybdenum: Characteristics, Production and Application*, ed. by M. Ortiz, T. Herrera (Nova Science, New York, 2012), pp. 147–179
6. W. Li, F. Xia, J. Qu, P. Li, D. Chen, Z. Chen, Y. Yu, Y. Lu, R.A. Caruso, Nano Res. **7**, 903 (2014)
7. M. Figlarz, Progr. Solid State Chem. **19**, 1 (1989)
8. C.-G. Wu, H.O. Marcy, D.C. DeGroot, C.R. Kannewurf, M.G. Kanatzidis, MRS Proc. **173**, 317 (1989)
9. C.-G. Wu, D.C. DeGroot, H.O. Marcy, J.L. Schindler, C.R. Kannewurf, Y.-J. Liu, W. Hirpo, M.G. Kanatzidis, Chem. Mater. **8**, 1992 (1996)
10. G. Du, K.H. Seng, Z. Guo, J. Liu, W. Li, D. Jia, C. Cook, Z. Liue, H. Liu, RSC Adv. **1**, 690 (2011)
11. F.J. Quites, C. Bisio, R.C.G. Vinhas, R. Landers, L. Marchese, H.O. Pastore, J. Colloid Interface Sci. **368**, 462 (2012)
12. D. Liu, Y. Liu, A. Pan, K.P. Nagle, G.T. Seidler, Y.-H. Jeong, G. Cao, J. Phys. Chem. C **115**, 4959 (2011)
13. K. Kalantar-zadeh, J.Z. Ou, T. Daeneke, A. Mitchell, T. Sasaki, M.S. Fuhrer, Appl. Mater. Today **5**, 73 (2016)

14. L. Peng, Y. Zhu, X. Peng, Z. Fang, W. Chu, Y. Wang, Y. Xie, Y. Li, J.J. Cha, G. Yu, Nano Lett. **17**, 6273 (2017)
15. A. Al-Temimy, B. Anasori, K.A. Mazzio, F. Kronast, M. Seredych, N. Kurra, M.-A. Mawass, S. Raoux, Y. Gogotsi, T. Petit, J. Phys. Chem. C (2020). https://doi.org/10.1021/acs.jpcc.9b11766
16. E.V. Skorb, D. Fix, D.V. Andreeva, D.G. Shchukin, H. Möhwald, Adv. Funct. Mater. **19**, 2373 (2009)
17. E.V. Skorb, D.G. Shchukin, H. Möhwald, D.V. Andreeva, Nanoscale **2**, 722 (2010)
18. D.V. Andreeva, D.V. Sviridov, A. Masic, H. Möhwald, E.V. Skorb, Small **8**, 820 (2012)
19. S. Stoll, A. Schweiger, J. Magn. Reson. **178**, 42 (2006)
20. E.A. Konstantinova, A.A. Minnekhanov, A.I. Kokorin, T.V. Sviridova, D.V. Sviridov, J. Phys. Chem. C **122**, 10248 (2018)
21. I. Nova, L. Lietti, L. Casagrande, L. Dall'Acqua, E. Giamello, P. Forzatti, Appl. Catal. B. **17**, 245 (1998)
22. A. Varlec, D. Arcon, S.D. Skapin, M. Remskar, Mater. Chem. Phys. **170**, 154 (2016)
23. T.V. Sviridova, LYu Sadovskaya, E.A. Konstantinova, N.A. Belyasova, A.I. Kokorin, D.V. Sviridov, Catal. Lett. **149**, 1147 (2019)
24. H.A. Kuska, M.T. Rogers, *ESR of First Row Transition Metal Complex Ions* (Interscience Publ, New York, 1968)
25. L. Lietti, I. Nova, G. Ramis, L. Dall'Acqua, G. Busca, E. Giamello, P. Forzatti, F. Bregani, J. Catal. **187**, 419 (1999)
26. M. Graetzel, R.F. Howe, J. Phys. Chem. **94**, 2566 (1990)
27. O.B. Lapina, A.A. Shubin, A.V. Nosov, E. Bosch, J. Spengler, H. Knolzinger, J. Phys. Chem. B **103**, 7599 (1999)
28. V.V. Smirnov, I.G. Tarkhanova, A.I. Kokorin, D.S. Tsvetkov, Kinet. Catal. **46**, 861 (2005)
29. A.I. Kokorin, Semicontuctors, in *Chemical Physics of Nanostructured*, ed. by A.I. Kokorin, D.W. Bahnemann (VSP–Brill Acad Publ, Utrecht, 2003), pp. 203–263
30. I.V. Kolbanev, E.N. Degtyarev, A.N. Streletskii, A.I. Kokorin, Appl. Magn. Reson. **47**, 575 (2016)
31. S.A. Al'tshuler, B.M. Kozyrev, *Electron Paramagnetic Resonance*, ed. by C.P. Poole, Jr. (Academic Press, New York, 1964)
32. YuN Molin, K.M. Salikhov, K.I. Zamaraev, *Spin Exchange* (Springer, Berlin, 1980)
33. A.I. Kokorin, V.M. Arakelyan, V.M. Arutyunyan, Russ. Chem. Bull. Intern. Ed. **52**, 93 (2003)
34. J.-P. Jolivet, M. Henry, J. Livage, *Metal Oxide Chemistry and Synthesis: From Solution to Solid State* (Wiley, Chichester, 2000)
35. V. Petkov, P.N. Trikalitis, E.S. Bozin, S.J.L. Billinge, T. Vogt, M.G. Kanatzidis, J. Am. Chem. Soc. **124**, 10157 (2002)
36. J.T. Szymanski, A.C. Roberts, Canad. Min. **22**, 681 (1984)
37. N. Noginova, F. Chen, T. Weaver, E.P. Giannelis, A.B. Bourlinos, V.A. Atsarkin, J. Phys. Condens. Matter **19**, 246208 (2007)
38. G. Vázquez-Victorio, U. Acevedo-Salas, R. Valenzuela, *Ferromagnetic Resonance Theory and Application* (IntechOpen, London, 2013)
39. S. Watanabe, S. Akutagawa, K. Sawada, T. Iwasa, Y. Shimoyama, Mater. Trans. **50**, 2187 (2009)
40. S.V. Yurtaeva, V.N. Efimov, G.G. Yafarova, A.A. Eremeev, V.S. Iyudin, A.A. Rodionov, K.L. Gainutdinov, I.V. Yatsyk, Appl. Magn. Reson. **47**, 555 (2016)
41. K. Vasić, Ž. Knez, E.A. Konstantinova, A.I. Kokorin, S. Gyergyek, M. Leitgeb, React. Funct. Polym. **148**, 104481 (2020)
42. L.G. Lavrenova, G.A. Bikzhanova, A.N. Bogatikov, P.N. Gaponik, J. Inorg. Chem. **41**, 587 (1996). **(in Russian)**